Orientation-selective spin-polarized edge states in monolayer NiI$_2$

Yu Wang[1,2,8], Xinlei Zhao[3,4,8], Li Yao[5], Huiru Liu [1,2], Peng Cheng [1,2], Yiqi Zhang [1,2], Baojie Feng [1,2] ✉, Fengjie Ma[4], Jin Zhao [5], Jiatao Sun [6] ✉, Kehui Wu [1,2,7] & Lan Chen [1,2,7] ✉

Spin-polarized edge states in two-dimensional materials hold promise for spintronics and quantum computing applications. Constructing stable edge states by tailoring two-dimensional semiconductor materials with bulk-boundary correspondence is a feasible approach. Recently layered NiI$_2$ is suggested as a two-dimensional type-II multiferroic semiconductor with intrinsic spiral spin ordering and chirality-induced electric polarization. However, the one-dimensional spin-polarized edge states of multiferroic materials down to monolayer limit has not yet been studied. We report here that monolayer NiI$_2$ was successfully synthesized on Au(111) by molecular beam epitaxy. Spin-polarized scanning tunneling microscopy/spectroscopy experiments visualize orientation-selective spin-polarized edge states in monolayer NiI$_2$ islands. By performing first-principles calculations, we further confirm that spin-polarized edge states are selectively aligning along the Ni-terminated edges rather than the I-terminated edges. Our result will provide the opportunity to tune edge states by selected orientation and to develop spintronic devices in two-dimensional magnetic semiconductors.

Edge states in two-dimensional (2D) systems can act as a unique one-dimensional (1D) conductive channel and play an important role in electron transport, which merits applications in spintronics and optoelectronics. For example, the quantum spin Hall effects in 2D topological insulators is endowed by the topological edge states exhibiting dissipationless electron transport channels[1]. Theoretically, when a homogeneous 2D electron gas is penetrated by a strong magnetic field, spin-polarized edge states will emerge[2], which can host pure 1D chiral current along the edges. Spin-polarized edge states have been reported in several 2D materials. For examples, pristine zigzag graphene nanoribbons have been confirmed to possess stable ferromagnetic coupling along the edge and antiferromagnetic coupling across the edge, which can be further tuned by edge modification[3–6]. Also, 1D magnetic metallic channels have been reported in MoS$_2$ nanoribbons and Mo edges of MoS$_2$ islands[7–9], and two symmetrical Pt edges in PtS$_2$ exhibit both metallic and magnetic properties with spin up and spin down configurations[10]. Moreover, as good candidates for the quantum anomalous Hall effect, magnetic topological insulators with spin-polarized chiral edge states[1,11–13] have been suggested to construct spintronics and quantum computing devices. However, the direct observation of spin-polarized edge states in intrinsic magnetic insulators is still rare.

Tailoring 2D materials with bulk-boundary correspondence is a fascinating and feasible approach for generating specific edge states, and it is more convenient than growing nanoribbons and

[1]Institute of Physics, Chinese Academy of Sciences, Beijing, China. [2]School of Physical Sciences, University of Chinese Academy of Sciences, Beijing, China. [3]State Key Laboratory of Low Dimensional Quantum Physics and Department of Physics, Tsinghua University, Beijing, China. [4]The Center for Advanced Quantum Studies and Department of Physics, Beijing Normal University, Beijing, China. [5]Department of Physics, University of Science and Technology of China, Hefei, Anhui, China. [6]School of Integrated Circuits and Electronics, MIIT Key Laboratory for Low-Dimensional Quantum Structure and Devices, Beijing Institute of Technology, Beijing, China. [7]Songshan Lake Materials Laboratory, Dongguan, Guangdong, China. [8]These authors contributed equally: Yu Wang, Xinlei Zhao. ✉e-mail: bjfeng@iphy.ac.cn; jtsun@bit.edu.cn; lchen@iphy.ac.cn

conventional 1D metal wires[14,15]. More importantly, edge states with exotic quantum properties could be tuned by precisely controlling the terminations and orientations of 2D materials. For example, 1D topologically nontrivial edge states can be obtained in 2D quantum spin Hall insulators when the bulk insulators are terminated by edges[16–18]. However, the realization of spin-polarized edge states in 2D materials with thickness down to the monolayer limit is still lacking and remains challenging.

2D transition metal dihalides MH_2 (M = V, Mn, Fe, Co, Ni; H = Cl, Br, I), with intrinsic band gap and magnetism[19–24], are possible candidates for magnetic topological materials[25]. Among them, monolayer NiI_2[20–23,26–34] as shown in Fig. 1a was recently suggested to be a 2D type-II multiferroic semiconductor[23], exhibiting proper-screw helix spin ordering and chirality-dependent electric polarization down to the monolayer limit[23]. Although the single-layer multiferroic NiI_2 have been studied by Raman spectroscopy, second harmonic generation (SHG) etc[35], it remains essentially unknown how the coupling between the spin ordering and electric polarization can persist along one-dimensional edge. In this work, we successfully synthesized NiI_2 monolayer on an iodine-modified Au(111) surface by molecular beam epitaxy (MBE) for the first time. Spin-polarized scanning tunneling microscopy/spectroscopy (SP-STM/STS) measurements revealed that significant spin-polarized 1D edge states occur at the Ni-terminated edges of NiI_2 islands rather than the I-terminated edges. Density functional theory (DFT) calculations show that the monolayer NiI_2 has broken three-fold symmetry due to the striped spin ordering giving rise to the orientation-selective spin-polarized edge states. Our results suggest that monolayer NiI_2 with orientation-selective spin-polarized edge states can not only act as a new platform for 2D obstructed atomic insulators, but may contribute to the development of spintronic devices and exotic quantum computing.

Results

Growth and atomic structure of monolayer NiI_2

In experiments, we grew NiI_2 on a clean Au(111) surface which exhibits a clear herringbone structure (Fig. 1b), by directly evaporating NiI_2 powder from a homebuilt evaporator. However, due to the easy decomposition of NiI_2 during growth when the source temperature increases, iodine atoms will first emerge from the evaporator and consequently be deposited on the Au(111) substrate, resulting in an iodine-covered Au(111) surface without the pristine herringbone reconstruction (Fig. 1c). High-resolution STM images taken on an iodine-covered Au(111) surface reveal two different structures in Supplementary Information Fig. S1a and S1b, which have been previously reported[36]. The pre-adsorption of iodine on Au(111) and the formation of iodine-modified Au(111) reconstruction [denoted by I/Au(111)] could eliminate the strain on the pristine Au(111) surface acting like buffer layer. Consequently, the successively grown 2D materials on such I/Au(111) surface can be expected to exhibit weaker interface interactions and retain most of their pristine physical properties.

As the source temperature increases, NiI_2 islands with hexagonal shape form on the I/Au(111) surface, as shown in the STM image of Fig. 1d, which exhibits two opposite orientations with respect to the Au(111) surface. The inset line profile implies that the height of the islands relative to I/Au(111) is ~6.8 Å, corresponding qualitatively to one monolayer thickness of the islands. The high-resolution STM images taken on the surface of the islands reveal hexagonal closely-packed protrusions with a lattice constant of a = 4.0 ± 0.05 Å and two stripes pattern within 9 × √3 supercell (Fig. 1e and Figure S1). It was recently proposed the spatial modulation of striped pattern arises possibly from the novel magnetic structure of one-dimensional spin spiral in multiferroic NiI_2 monolayer as shown in Fig. 1f[37,38]. The possibility that the moiré structure is the origin of 9 × √3 supercell is excluded by the
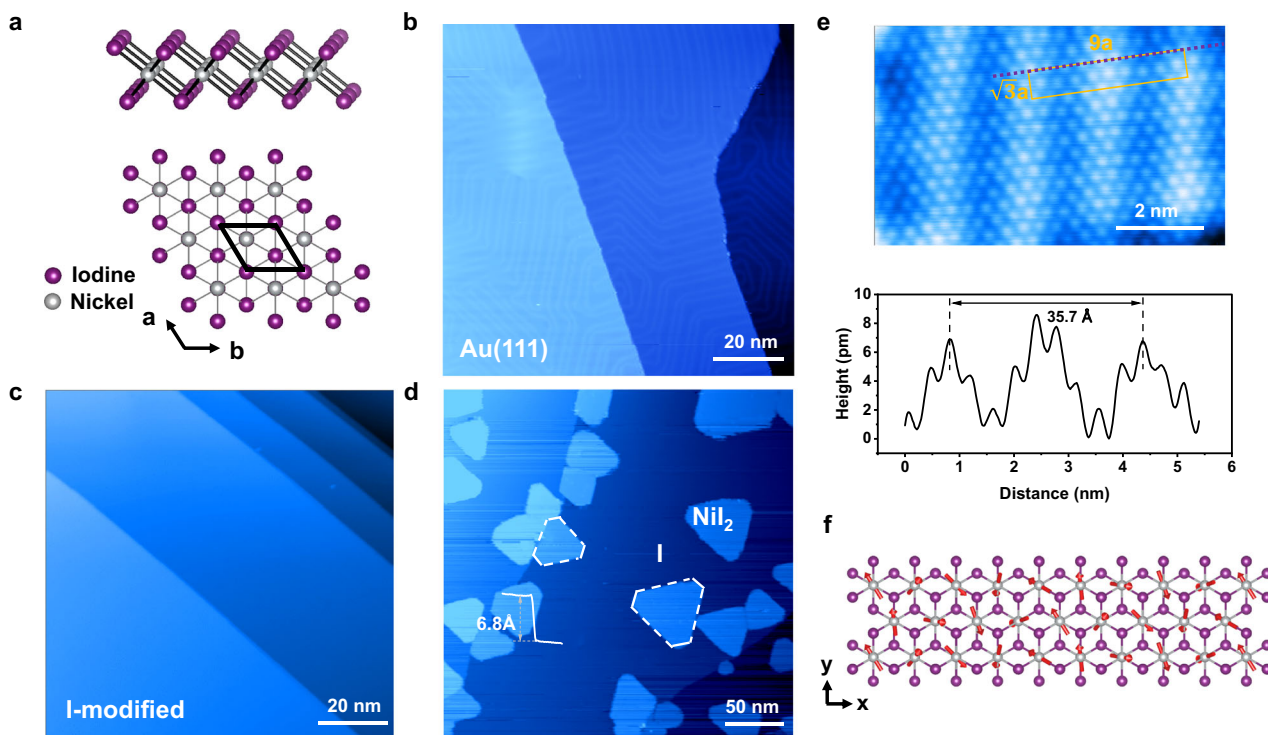

Fig. 1 | Monolayer NiI_2 islands grown on iodine modified Au(111). a Side view and top view of the crystal structure of monolayer NiI_2. **b** Topography of the Au(111) surface reconstructions with herringbone pattern (100×100 nm²; $V_s = -3.0$ V, $I_s = 50$ pA). **c** STM image of iodine modified Au(111) (100×100 nm²; $V_s = -1.0$ V, $I_s = 50$ pA). **d** Topography of NiI_2 monolayer islands on I/Au(111) substrate (300×300 nm²; $V_s = 1.1$ V, $I_s = 50$ pA). The white dotted lines outline the shapes of the NiI_2 islands. **e, f** Atomically resolved STM topographic image with Cr tip and top view of the crystal structure of monolayer NiI_2 with spin spiral order. Line profile along purple line in atomic-resolution image. The spin directions are labeled by red arrows.
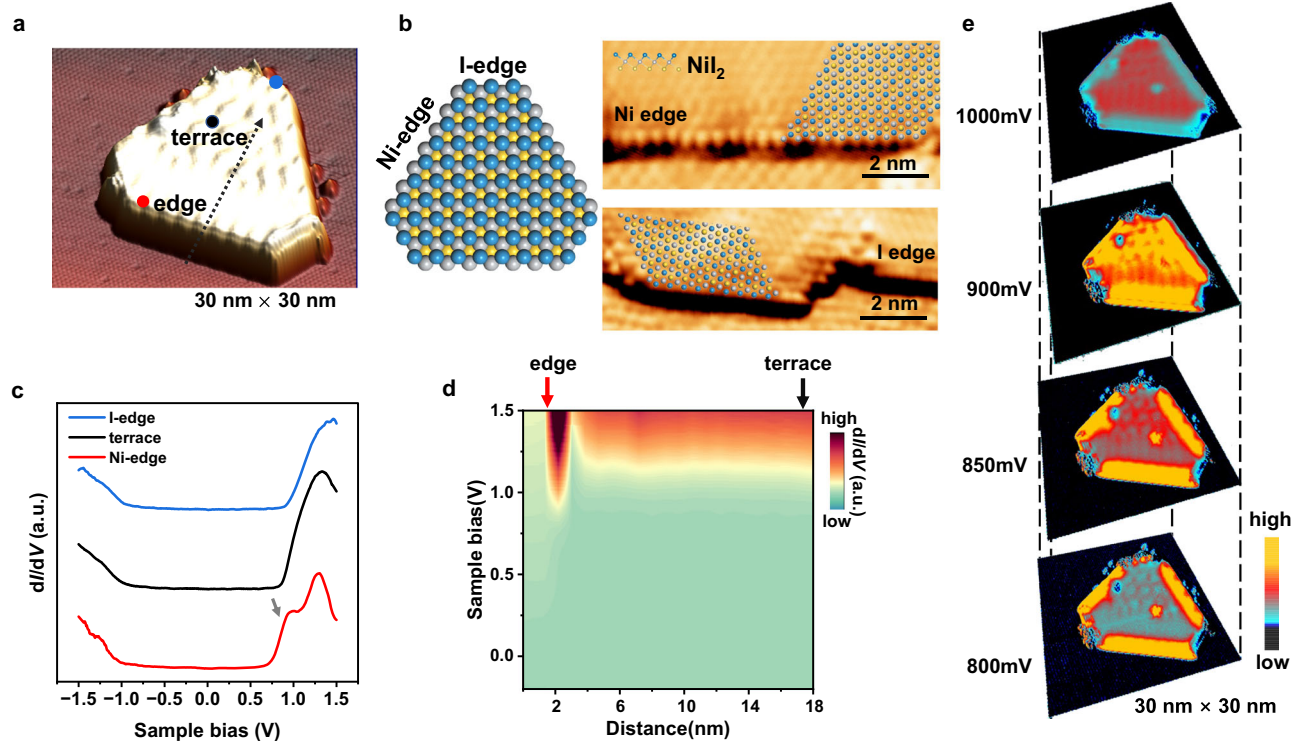
Fig. 2 | The orientation-selected edge states of an NiI$_2$ island measured with a W tip. a STM image of monolayer NiI$_2$ island with hexagonal shape ($V_s = 0.3$ V, $I_s = 100$ pA). **b** Top view of ball model and high-resolution STM images of hexagonal NiI$_2$ island terminated by Ni-edges and I-edges ($V_s = 0.5$ V, $I_s = 100$ pA). The overlying atomic model is denoted by colors: I$_{top}$: blue; Ni: gray; I$_{bottom}$: yellow. **c** dI/dV spectra taken in the Ni-edge, interior terrace, and I-edge of the NiI$_2$ island in (**a**). The gray arrow indicates the position of the edge state. **d** Spatially resolved dI/dV map along the black dotted lines shown in (**a**). **e** Vertically stacked dI/dV mappings of the same NiI$_2$ island depending on different sample bias voltages.

continuous visualization of stripes across the substrate steps [Supplementary Information Fig. S2]. Combining the island height and the lattice constant, we infer that these islands are NiI$_2$ monolayers, and that the atoms on the island surface are iodine atoms. The top sublayer consists of iodine atoms due to the I-Ni-I crystal structure, which is consistent with previous reports[19,22,23,26]. To further confirm the composition of the sample, we have performed X-ray photoelectron spectroscopy (XPS) measurements on monolayer sample on I/Au and NiI$_2$ powder. The binding energy peaks of Ni-2$p_{3/2}$, I-3$p_{3/2}$, I-3d and Au-4f of sample are shown in Supplementary Information Fig. S3. The results of XPS showed that the binding energy peak shapes and energy positions of Ni and I in sample as same as those in NiI$_2$ powder, and are consistent with previous reports[39,40]. Hence, we confirmed that the islands on I/Au surface was NiI$_2$.

STS measurements of orientation-selective spin-polarized edge states

To reveal the electronic structures of monolayer NiI$_2$, we performed STS measurements on monolayer NiI$_2$ island with W tip. Figure 2a shows a hexagonal NiI$_2$ island exhibiting alternating edge length. Since the surface atoms resolved by atomic-resolution STM images should be top-layer iodine atoms according to the I-Ni-I crystal structure, we can superimpose the atomic model of NiI$_2$ on the atomic-resolution STM images of NiI$_2$ islands with different edges, then determine the types of terminated atoms. According to the atomic-resolution images of the island edges of NiI$_2$, we can conclude that there are two kinds of zigzag edges in such hexagonal NiI$_2$ islands (Fig. 2b): Ni-edge and I-edge, corresponding to the long and short edges in Fig. 2a respectively. The line profiles across the I-edge and Ni-edge of NiI$_2$ island in Fig. 2b and the results are shown in Supplementary Information Figure S4. The distinct line profiles across the edges can distinguish different terminated atoms. The dI/dV spectrum taken on the terrace of NiI$_2$ islands shows a

characteristic gap of 1.65 eV, with the conduction band minimum (CBM) located about 850 meV above the Fermi level (Fig. 2c).

The STS of Ni-edge shows an extra shoulder in the density of states (DOS) at 700–900 meV with considerably higher intensities than on the terrace, suggesting the existence of edge states at the Ni-edge. In contrast, STS images taken at the I-edge show the same feature as on the terrace, and there is no extra shoulder of DOS. Therefore, the edge state shows distinctive orientation selectivity. The evolution of the edge states in real space is also illustrated in the color map in Fig. 2d, which consists of a series of dI/dV curves acquired along a line across Ni-edge of the NiI$_2$ island. A prominent edge state occurs at Ni-edges at 700–900 meV, while the DOS of the inner terrace is weak and spatially homogenous. The energy window of this delineated edge state is about 200 meV.

Figure 2e shows the corresponding dI/dV mappings of the same NiI$_2$ island taken at a series of sample biases. The significant edge states can be observed at the three symmetrical Ni-edges in the energy range 800–900 meV above the Fermi level, but are absent at the I-edges. The penetration depth of edge state across the Ni-edges is about 2 nm, indicating that the distribution of edge states in NiI$_2$ exhibits a certain degree broadening in real space. Factors such as the electronic wave function distribution and the decay behavior of the edge states could contribute to this characteristic penetration depth in the STS measurements. When the bias is above 1 eV, the edge states immerse within the bulk states and can't be distinguished. Orientation-selective edge states can also be observed simultaneously on two neighboring islands with opposite orientations, as shown in Supplementary Information Fig. S5.

Furthermore, we performed SP-STM experiments to detect the spin-polarized edge states of monolayer NiI$_2$ using Cr tip. Before characterizing the NiI$_2$ island with Cr tip, we first checked the spin polarized ability of Cr tip on the Cr(100) surface, in which the neighbor
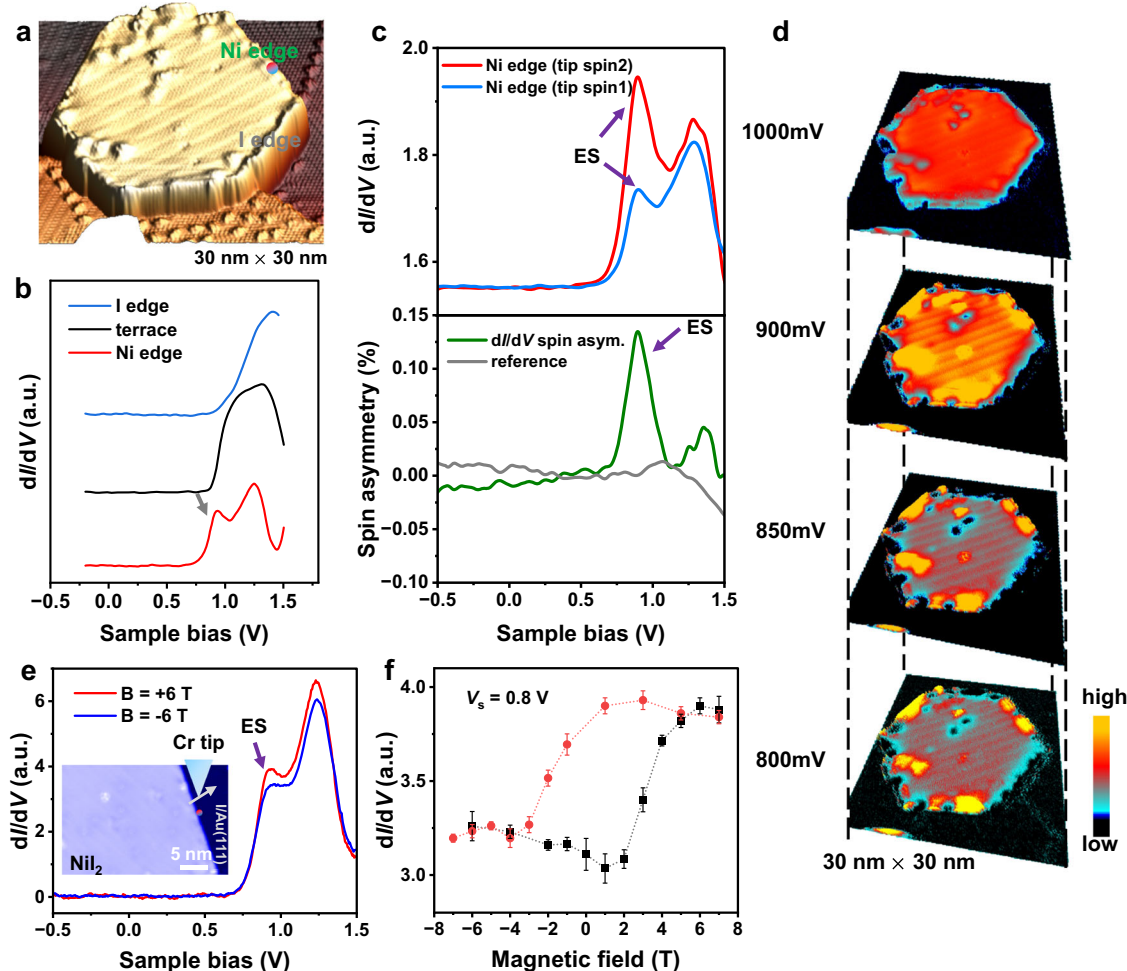
Fig. 3 | The orientation-selected spin-polarized edge states of an NiI$_2$ island measured with a Cr tip. a SP-STM image of monolayer NiI$_2$ island with stripe modulation ($V_s = 0.87$ V, $I_s = 100$ pA). **b** dI/dV spectra taken in the Ni-edge, interior terrace, and I-edge of the NiI$_2$ island. The gray arrow indicates the position of the edge state. **c** Spin resolved point spectroscopy at the Ni-edge position indicated by red with blue point in (**a**) for the tip spin state 1 (blue curve) and tip spin state 2 (red curve). The resulting energy-resolved spin polarization is given by the green curve in the bottom panel of (**c**). Light grey curve represent the background asymmetry obtained over I-edge (reference). **d** Vertically stacked dI/dV mappings of the same NiI$_2$ island depending on different sample bias voltages. **e** Spin-polarized tunneling spectra at positive and negative out-of-plane magnetic fields (±6 T) obtained on one position in the inset. The inset indicates the STM image of NiI$_2$ island with Ni-edge. **f** dI/dV signal as a function of the magnetic field at $V_s = 0.8$ V. The out-of-plane magnetic field was swept upward (black points) and downward (red points). Error bar indicate the resolution of the differential conductance in the measurement. The hysteresis loop is fitted as dot lines.

Cr layers have a antiparallel spin orientation [Supplementary Information Fig. S6]. Figure 3a illustrates a hexagonal NiI$_2$ island exhibiting a spin spiral with stripe modulation, and the stripe modulation can extend to the edges of NiI$_2$ island. The six edges of the NiI$_2$ island are composed of alternating Ni-edge and I-edge, as observed in the island in Fig. 2a. The STS of Ni-edge by Cr tip still reveals an additional peak at about 0.9 eV, signifying the existence of edge states at the Ni-edge, whereas no such states are observed at the I-edge (Fig. 3b). Therefore, the clear orientation selectivity of the edge states in NiI$_2$ is a prevalent phenomenon. Referring to the detection method of spin-polarized edge states in other systems[41–43], we measured the dI/dV spectra [state 1 (Ni$_1$): blue curve and state 2 (Ni$_2$): red curve] on Ni-edges at two different tip spin states (tip state 1 and 2), as show in top panel of Fig. 3c. Then we set the dI/dV spectra taken at I-edge as a reference signal at a certain tip spin state [light grey curve in Fig. 3c], and calculated spin asymmetry of Ni-edge state (S$_a$) through taking the difference of the dI/dV signal divided by the corresponding reference [S$_a$ = (Ni$_2$-I$_2$)/I$_2$ – (Ni$_1$-I$_1$)/I$_1$, green curve in Fig. 3c]. The distinct spin asymmetry of the edge states indicates that the edge states are spin-polarized, as shown in bottom panel of Fig. 3c. For comparison, we recorded the dI/dV signals on Ni-edge and I-edge by W tip with two

different tip states, then calculated the spin asymmetry using the same method with Cr tip. The results are shown in Supplementary Information Figure S7. The spin asymmetry of Ni-edges is quite small at two different tip states, which is significantly different from those obtained by Cr tip with different tip states, suggesting the presence of spin tunneling current. Figure 3d shows the corresponding dI/dV mappings of the NiI$_2$ island in Fig. 3a. The edge states can be observed at the three symmetrical Ni-edges in the energy range from 800 meV to 900 meV, but are absent at the I-edges. Meanwhile, the spin spiral stripe modulation of the terrace extends to the edges. There is always defect on the edges of NiI$_2$ islands, and the edge defects affect the spin states and edge states. Figure 3d indicates an island with defects on edge, which exhibits the modulation stemmed from spin spiral configurations. We can observe the presence of defects along the Ni-edges of the NiI$_2$ island, which induces in the discontinuity of edge states along the edge. Additionally, the spin-polarization modulation is also influenced in areas where defects occur on the terrace and edges.

Furthermore, we performed the SP-STM experiment under external magnetic fields. Figure 3e shows the dI/dV curves taken on the Ni-edge of a monolayer NiI$_2$ island with oppositely applied magnetic fields (B = ± 6 T). It is obvious that the edge state intensity is changed

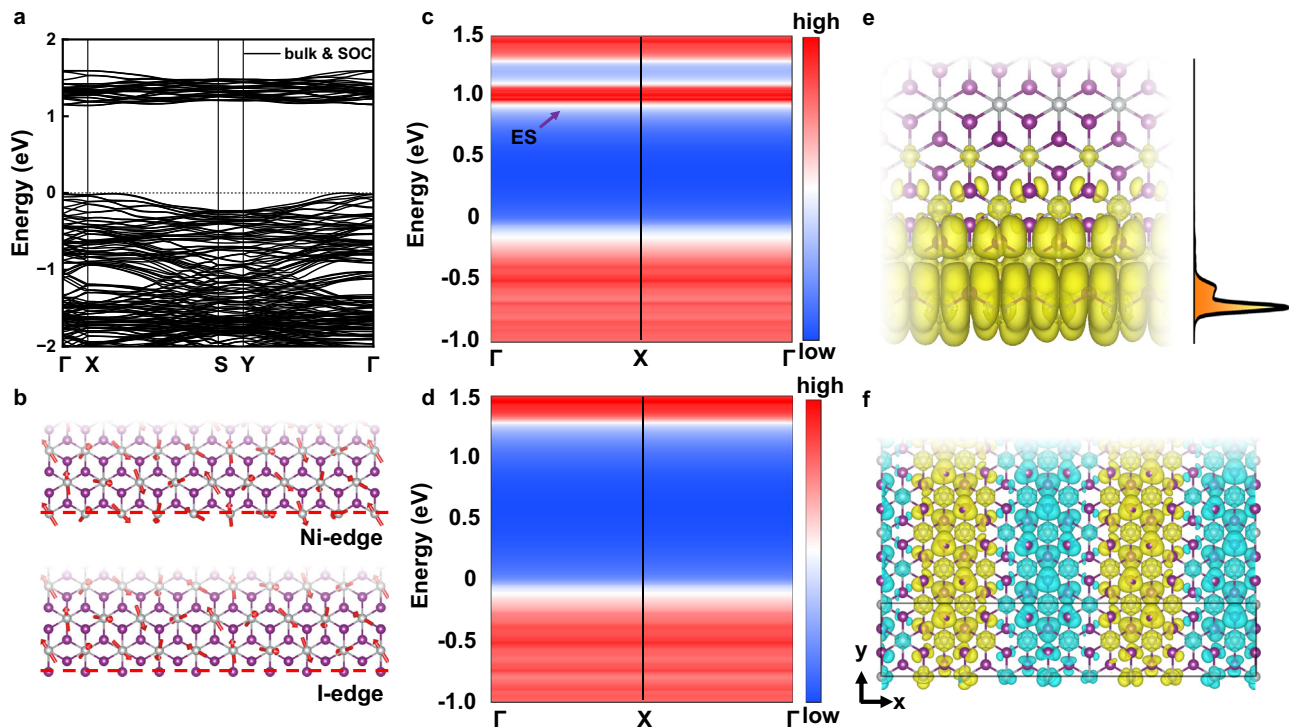**Fig. 4 | The calculated electronic states of NiI_2 monolayer and nanoribbon.**
a Band structures of NiI_2 monolayer with SOC included in the $4.5 \times \sqrt{3}$ spin spiral state. **b** The upper and lower panels show the edge geometric structures and magnetic structures of zigzag nanoribbons terminated by Ni and I atoms, respectively. The spin orientations of each Ni atom are labeled by red arrows. The edge states for the freestanding NiI_2 nanoribbons with **c** Ni-terminated edges and **d** I-terminated edges. The edge states are marked by purple arrow. **e** The distribution of partial charge density of the Ni-terminated edge states at the Γ point as denoted by purple arrow in **c**. The isosurface is set to 1×10^{-6} e/Å³. The planar-averaged charge density across the nanoribbon width is shown in the right part of (**e**). **f** The distribution of magnetization density of the nanoribbons in the spin-spiral state. The yellow and cyan contours represent positive and negative moments along the x direction, respectively. The isosurface is set to 1.5×10^{-3} e/Å³.

under reversed magnetic field, confirming the existence of spin-polarized tunneling current. Furthermore, a series of dI/dV spectra are obtained as the magnetic field (±7 T) is sweeping forth and back. Figure 3f shows the edge state intensity ($V_s = 0.8$ V) as a function of magnetic field. We can observe a hysteresis loop with two approximate plateaus corresponding to two spin-polarized states, exhibiting a similar ferromagnetic hysteresis. Additionally, the dI/dV plateaus is sensitively depend on several parameters such as bias, atomic sites and Cr tip states[44]. Combining the above STS results with external magnetic field, we believe that the edge states of NiI_2 island is spin-polarized.

First-principles calculations of edge states

To understand the orientation selectivity of the edge states, we performed first-principles calculations on an NiI_2 monolayer and on nanoribbons. We chose experimental lattice constants of the monolayer NiI_2 to construct the primitive cell. As a type-II multiferroic materials in bulk form, the nature of spin ordering and electric polarization in ultimate limit of NiI_2 monolayer is recently under hot debate[20–24,26–33]. Then in the spirit of previous reports[23,33], we first studied the ground state by choosing a variety of spin ordering in DFT calculations, including ferromagnetic (FM), collinear-antiferromagnetic (collinear-AFM), bicollinear-AFM (bc-AFM), zigzag-AFM and in plane 7×1 spin spiral order, in plane $9 \times \sqrt{3}$ spin spiral order, canted plane $4.5 \times \sqrt{3}$ spin spiral order, as shown in Supplementary Information Figure S8. If the energy of $4.5 \times \sqrt{3}$ spin spiral state is set as a reference, the relative energies with respect to other spin configurations are listed in Supplementary Information Table S1. Clearly, the $4.5 \times \sqrt{3}$ spin spiral state with broken three-fold rotational symmetry has lower energy, which agree well with the latest work[38].

First-principles calculations show that the band gap of NiI_2 is smaller than the STS measurements. The Hubbard's $U = 4.2$ eV and Hund's exchange coupling constant $J = 0.8$ eV for Ni $3d$ orbitals are adopted in the following, according to the references[33,38]. The calculated magnetic moment is $1.42\,\mu_B$ per Ni mainly from Ni $3d$ orbitals. Figure 4a shows the band structures of NiI_2 in the $4.5 \times \sqrt{3}$ spin spiral state with spin orbit coupling (SOC). It is clear that the NiI_2 monolayer is a insulator with a large band gap of 1.2 eV.

We then calculated the band structures by constructing zigzag NiI_2 nanoribbons terminated by two kinds of edges (Ni-terminated and I-terminated) as shown in Fig. 4b. The relaxed magnetic structure of the nanoribbon edge, reveal that the magnetic structure of the edge atoms maintains the spin spiral order, which is consistent with the bulk state. From the band structures of the Ni-terminated nanoribbon (Fig. 4c), it is clear that there are unoccupied edge states completely disentangled with higher energy bands throughout the Brillouin zone (BZ) located near the bottom of the conduction band. In contrast, the band structures of the I-terminated nanoribbon has a clean band gap without additional states (Fig. 4d), indicating that the edge states of monolayer NiI_2 have a clear orientation selectivity. In addition, the emergence of edge states is related to the edge termination rather than spin configurations. At the NiI_2 island edge, the Ni atoms at the Ni-edge are exposed, with their unfilled d orbitals forming an unsaturated bond state. Excess electrons are thus prone to forming dangling bonds. The edge states obtained in calculations are including the status of dangling bonds. We have also added the results of bc-AFM, FM and in plane $9 \times \sqrt{3}$ spin spiral states calculations to the Supplementary Information Fig. S9–S11, showing that such edge states can also be provided. Figure 4e shows the real spatial distribution of charge density of the edge states, which are clearly localized at the edges of the Ni-

terminated nanoribbon. The right panel of Fig. 4e shows the planar-averaged charge density across the nanoribbon, which exhibit the penetration width of 1.0 nm resembling to the broadening width of localized states shown in Fig. 2e. The distribution of magnetization density of the nanoribbon (Fig. 4f) shows a periodic stripe modulation in both the edge and bulk states, indicating that they have the same magnetic structure, which is consistent with the experimental observation and the optimization calculation of the magnetic structure. Therefore, the 1D edge states of the NiI_2 monolayer terminated by Ni atoms are spin-polarized panetrating the spin spiral state far beyond nanometer agreeing with the experimental observation of stripe pattern. Due to the broken inversion symmetry from the spin spiral ordered magnetic structure, NiI_2 monolayer exhibits ferroelectric polarization characterized by real-space modulation of magnetization state.

Further discussions on orientation-selective edge states in 2D trivial insulator

Recently, Xu et al.[45,46] provided the full classification of three-dimensional (3D) obstructed atomic insulators (OAIs) by the real space invariants (RSIs) in 3D topologically trivial insulators. All of them present a filling anomaly under certain open-boundary conditions and exhibit obstructed surface states (OSSs) or higher order obstructed edge states (OESs)[45–48]. Although the spin-polarized edge states shown in Fig. 4c, e are topologically trivial without bulk-boundary correspondence, the exotic magnetic configuration breaking the inversion symmetry of atomic structure provide new possibility to tune the polarization in the monolayer limit. Moreover, the edge states in NiI_2 throughout the 1D BZ disentangling with the higher conduction band and lower valence bands show similar behaviors with OESs in Maxene systems like $MoSi_2N_4$[47] and breathing Kagome systems like Nb_3TeCl_7[49], which offers a potential platform for realizing 2D OAI and higher order topological states. The disentanglement of edge states with inherently large gaps provides a noise-free background for experimental development of ultra-low dissipation spintronic devices. In addition to cutting off two types of atoms on crystal structure, it is also possible to manipulate the edge states by doping other elements (substitution atoms) during growth to modify crystal structures[50,51]. The potential applications of 2D OAI on catalysis[48] and superconductivity[52] will have the opportunity to extend the applications of spin-polarized edge states of monolayer NiI_2, which may serve as a 1D catalytic active site[53] or a 1D topological superconductivity[54,55].

Discussion

In summary, we have successfully synthesized the monolayer NiI_2 islands on an iodine-modified Au(111) substrate. SP-STM/STS measurements and first-principles calculations reveal that spin-polarized edge states exist at the Ni-terminated edges but not at the I-terminated edges in monolayer NiI_2. The edge states of NiI_2 have well-defined orientation selectivity and spin-polarization. This result will be beneficial for tuning edge states by edge modification and it has potential applications in the development of spintronic devices in 2D magnetic insulators. Furthermore, the unique edge states that rely on specific cutoff edges in topologically trivial systems allow the use of NiI_2 to provide insight into the study of OAI materials.

Methods

Sample fabrication and SP-STM/STS characterization

The experiments were performed in a homebuilt low-temperature STM with an MBE system (base pressure ~10^{-8} Pa). The iodine was first evaporated onto a clean Au(111) substrate by using a homebuilt evaporator (NiI_2 powder, 99.5%). Then NiI_2 powder was evaporated onto the iodine-modified Au(111) substrate by slightly increasing the evaporation temperature of the evaporator and was annealed at

~100°. After growth, the sample was transferred to an STM chamber without breaking the vacuum. All the STM and spin-polarized STM images were taken at 5 K using an electrochemically etched W tip and Cr tip. The tip states are changed by applying the pulse voltage. We performed in situ spin-polarized STM measurements with an applied out-of-plane magnetic field at 4.6 K in the Unisoku STM (1300) system. The STS spectra were taken by using a lock-in amplifier with a modulation voltage from 10 to 20 mV at a frequency of 667 Hz. The STM/STS data were processed using free WSxM software[56].

Theoretical calculations

Calculations were performed using the plane-wave basis set as implemented in the Vienna ab initio simulation package (VASP) software package[57,58]. The generalized gradient approximation (GGA) of the Perdew-Burke-Ernzerhof (PBE) formulation was used to calculate the exchange-correlation potentials in the electronic structure calculations[59]. The projector augmented wave (PAW) method was employed to model the electron-ion interactions[60,61]. The effective on-site Coulomb U and exchange interactions J, were introduced to treat the strong correlation of the localized electrons of the transition metal ions[62–64]. The effective values of U and J applied on Ni $3d$ electrons were 4.2 eV and 0.8 eV, respectively. A k mesh of $1 \times 6 \times 1$ was used to sample the whole Brillouin zone (BZ), and a Gaussian smearing of 0.05 eV was adopted for the Fermi surface broadening. After convergence tests, the kinetic-energy cutoff of the plane-wave basis was set to be 500 eV. The total energy convergence and the atomic force tolerance were set to 10^{-5} eV and 0.01 eV/Å, respectively. The edge states were studied using tight-binding methods by the combination of Wannier90[65] and WannierTools[66] software packages.

Data availability

The data that support the findings of this paper are available from the corresponding authors upon request.

References

1. Wang, J., Lian, B. & Zhang, S.-C. Quantum anomalous Hall effect in magnetic topological insulators. *Phys. Scr. T* **164**, 014003 (2015).
2. Hornberger, K. & Smilansky, U. Magnetic edge states. *Phys. Rep.* **367**, 249–385 (2002).
3. Yazyev, O. V., Capaz, R. B. & Louie, S. G. Theory of magnetic edge states in chiral graphene nanoribbons. *Phys. Rev. B* **84**, 115406 (2011).
4. Son, Y.-W., Cohen, M. L. & Louie, S. G. Half-metallic graphene nanoribbons. *Nature* **444**, 347–349 (2006).
5. Kunstmann, J., Özdoğan, C., Quandt, A. & Fehske, H. Stability of edge states and edge magnetism in graphene nanoribbons. *Phys. Rev. B* **83**, 045414 (2011).
6. Slota, M. et al. Magnetic edge states and coherent manipulation of graphene nanoribbons. *Nature* **557**, 691–695 (2018).
7. Li, Y., Zhou, Z., Zhang, S. & Chen, Z. MoS_2 nanoribbons: high stability and unusual electronic and magnetic properties. *J. Am. Chem. Soc.* **130**, 16739–16744 (2008).
8. Helveg, S. et al. Atomic-scale structure of single-layer MoS_2 nanoclusters. *Phys. Rev. Lett.* **84**, 951–954 (2000).
9. Bollinger, M. V. et al. One-dimensional metallic edge states in MoS_2. *Phys. Rev. Lett.* **87**, 196803 (2001).
10. Liu, S., Zhu, H., Liu, Z. & Zhou, G. Symmetrical metallic and magnetic edge states of nanoribbon from semiconductive monolayer PtS_2. *Phys. Lett. A* **382**, 776–780 (2018).
11. Yu, R. et al. Quantized anomalous Hall effect in magnetic topological insulators. *Science* **329**, 61–64 (2010).
12. Chang, C.-Z. et al. Experimental observation of the quantum anomalous Hall effect in a magnetic topological insulator. *Science* **340**, 167–170 (2013).

13. Gong, Y. et al. Experimental realization of an intrinsic magnetic topological insulator. *Chin. Phys. Lett.* **36**, 076801 (2019).

14. Snijders, P. C., Johnson, P. S., Guisinger, N. P., Erwin, S. C. & Himpsel, F. J. Spectroscopic evidence for spin-polarized edge states in graphitic Si nanowires. *N. J. Phys.* **14**, 103004 (2012).

15. Oncel, N. et al. Quantum confinement between self-organized Pt nanowires on Ge(001). *Phys. Rev. Lett.* **95**, 116801 (2005).

16. Drozdov, I. K. et al. One-dimensional topological edge states of bismuth bilayers. *Nat. Phys.* **10**, 664–669 (2014).

17. Peng, L. et al. Visualizing topological edge states of single and double bilayer Bi supported on multibilayer Bi(111) films. *Phys. Rev. B* **98**, 245108 (2018).

18. Zhao, C. et al. Coexistence of Robust Edge States and Superconductivity in Few-Layer Stanene. *Phys. Rev. Lett.* **128**, 206802 (2022).

19. Kuindersma, S. R., Sanchez, J. P. & Haas, C. Magnetic and structural investigations on NiI_2 and CoI_2. *Phys. B* **111**, 231–248 (1981).

20. Botana, A. S. & Norman, M. R. Electronic structure and magnetism of transition metal dihalides: Bulk to monolayer. *Phys. Rev. Mater.* **3**, 044001 (2019).

21. Lu, M., Yao, Q., Xiao, C., Huang, C. & Kan, E. Mechanical, electronic, and magnetic properties of NiX_2 (X = Cl, Br, I) Layers. *ACS Omega* **4**, 5714–5721 (2019).

22. Liu, H. et al. Vapor Deposition of magnetic Van der Waals NiI_2 crystals. *ACS Nano* **14**, 10544–10551 (2020).

23. Song, Q. et al. Evidence for a single-layer van der Waals multiferroic. *Nature* **602**, 601–605 (2022).

24. An, Y. et al. Spin transport properties and nanodevice simulations of NiI_2 monolayer. *Phys. E* **142**, 115262 (2022).

25. Chen, P., Zou, J.-Y. & Liu, B.-G. Intrinsic ferromagnetism and quantum anomalous Hall effect in a $CoBr_2$ monolayer. *Phys. Chem. Chem. Phys.* **19**, 13432 (2017).

26. Ju, H. et al. Possible persistence of multiferroic order down to bilayer limit of van der Waals material NiI_2. *Nano Lett.* **21**, 5126–5132 (2021).

27. Fumega, A. & Lado, J. L. Microscopic origin of multiferroic order in monolayer NiI_2. *2D Mater.* **9**, 025010 (2022).

28. Wang, Y. et al. Three-dimensional real space invariants, obstructed atomic insulators and a new principle for active catalytic sites. *npj Comput. Mater.* **8**, 218 (2022).

29. Li, X., Zhang, Z. & Zhang, H. High throughput study on magnetic ground states with Hubbard U corrections in transition metal dihalide monolayers. *Nanoscale Adv.* **2**, 495 (2020).

30. Kulish, V. V. & Huang, W. Single-layer metal halides MX_2 (X = Cl, Br, I): stability and tunable magnetism from first principles and Monte Carlo simulations. *J. Mater. Chem. C.* **5**, 8734 (2017).

31. Han, H., Zheng, H., Wang, Q. & Yan, Y. Enhanced magnetic anisotropy and Curie temperature of the NiI_2 monolayer by applying strain: a first-principles study. *Phys. Chem. Chem. Phys.* **22**, 26917 (2020).

32. Dong, X. J., Ren, M. J. & Zhang, C. W. Quantum anomalous Hall effect in germanene by proximity coupling to a semiconducting ferromagnetic substrate NiI_2. *Phys. Chem. Chem. Phys.* **24**, 21631 (2022).

33. Liu, N. et al. Competition Multiferroic Phases in monolayer and few-layer NiI_2. *Phys. Rev. B* **109**, 195422 (2024).

34. Komarov, N. S., Pavlova, T. V. & Andryushechkin, B. V. New atomic-scale insights into the I/Ni(100) system: phase transitions and growth of an atomically thin NiI_2 film. *Phys. Chem. Chem. Phys.* **23**, 1896 (2021).

35. Nordlander, J. et al. The ultrathin limit of improper ferroelectricity. *Nat. Commun.* **10**, 5591 (2019).

36. Huang, L., Zeppenfeld, P., Horch, S. & Comsa, G. Determination of iodine adlayer structures on Au(111) by scanning tunneling microscopy. *J. Chem. Phys.* **107**, 585 (1997).

37. Amini, M. Atomic-scale visualization of multiferroicity in monolayer NiI_2. *Adv. Mater.* **36**, 2311342 (2024).

38. Miao, M.-P. et al. Spin-resolved imaging of atomic-scale helimagnetism in monolayer NiI_2. Preprint at https://doi.org/10.48550/arXiv.2309.16526 (2023).

39. Matienzo, L. J., Yin, L. I., Grim, S. O. & Swartz, W. E. X-Ray Photoelectron Spectroscopy of Nickel Compounds. *Inorg. Chem.* **12**, 2763 (1973).

40. Biesinger, M. C., Lau, L. W. M., Gerson, A. R., Smart, R. & St, C. The role of the Auger parameter in XPS studies of nickel metal, halides and oxides. *Phys. Chem. Chem. Phys.* **14**, 2434 (2012).

41. Brede, J. et al. Detecting the spin-polarization of edge states in graphene nanoribbons. *Nat. Commun.* **14**, 6677 (2023).

42. Corbetta, M. et al. Magnetic Response and Spin Polarization of Bulk Cr Tips for In-Field Spin-Polarized Scanning Tunneling Microscopy. *Jpn. J. Appl. Phys.* **51**, 030208 (2012).

43. Ferriani, P., Lazo, C. & Heinze, S. Origin of the spin polarization of magnetic scanning tunneling microscopy tips. *Phys. Rev. B* **82**, 054411 (2010).

44. Chen, W. et al. Direct observation of van der Waals stacking–dependent interlayer magnetism. *Science* **366**, 983 (2019).

45. Xu, Y. et al. Three-Dimensional Real Space Invariants, Obstructed Atomic Insulators and A New Principle for Active Catalytic Sites. Preprint at https://doi.org/10.48550/arXiv.2111.02433 (2021).

46. Xu, Y. et al. Filling-Enforced Obstructed Atomic Insulators. *Phys. Rev. B* **109**, 165139 (2024).

47. Wang, L. et al. Two-dimensional obstructed atomic insulators with fractional corner charge in the MA_2Z_4 family. *Phys. Rev. B* **106**, 155144 (2022).

48. Li, G. et al. Obstructed Surface States as the Descriptor for Predicting Catalytic Active Sites in Inorganic Crystalline Materials. *Adv. Mater.* **34**, 2201328 (2022).

49. Zhou, H. et al. Orbital degree of freedom induced multiple sets of second order topological states in two-dimensional breathing Kagome crystals. *npj Quantum Mater.* **8**, 16 (2023).

50. Grønborg, S. S. et al. Visualizing hydrogen-induced reshaping and edge activation in MoS_2 and Co-promoted MoS_2 catalyst clusters. *Nat. Commun.* **9**, 2211 (2018).

51. Wang, Y. et al. Real-space detection and manipulation of two-dimensional quantum well states in few-layer MoS_2. *Phys. Rev. B* **105**, L081404 (2022).

52. Wu, H. et al. The field-free Josephson diode in a van der Waals heterostructure. *Nature* **604**, 653–656 (2022).

53. Ni, B. & Wang, X. Face the Edges: Catalytic Active Sites of Nanomaterials. *Adv. Sci.* **2**, 1500085 (2015).

54. Wang, Y., Lee, G.-H. & Ali, M. N. Topology and superconductivity on the edge. *Nat. Phys.* **17**, 542–546 (2021).

55. Pribiag, V. S. et al. Edge-mode superconductivity in a two-dimensional topological insulator. *Nat. Nanotechnol.* **10**, 593–597 (2015).

56. Horcas, I. et al. WSxM: a software for scanning probe microscopy and a tool for nanotechnology. *Rev. Sci. Instrum.* **78**, 013705 (2007).

57. Kresse, G. & Furthmüller, J. Efficient iterative schemes for ab initio total-energy calculations using a plane-wave basis set. *Phys. Rev. B* **54**, 11169 (1996).

58. Kresse, G. & Furthmüller, J. Efficiency of ab-initio total energy calculations for metals and semiconductors using a plane-wave basis set. *Comp. Mater. Sci.* **6**, 15 (1996).

59. Perdew, J. P., Burke, K. & Ernzerhof, M. Generalized Gradient Approximation Made Simple. *Phys. Rev. Lett.* **77**, 3865 (1996).

60. Blöchl, P. E. Projector augmented-wave method. *Phys. Rev. B* **50**, 17953 (1994).

61. Kresse, G. & Joubert, D. From ultrasoft pseudopotentials to the projector augmented-wave method. *Phys. Rev. B* **59**, 1758 (1999).

62. Liechtenstein, A. I., Anisimov, V. I. & Zaanen, J. Density-functional theory and strong interactions: Orbital ordering in Mott-Hubbard insulators. *Phys. Rev. B* **52**, R5467 (1995).
63. Cococcioni, M. & Gironcoli, S. Linear response approach to the calculation of the effective interaction parameters in the LDA + U method. *Phys. Rev. B* **71**, 035105 (2005).
64. Himmetoglu, B., Wentzcovitch, R. M. & Cococcioni, M. First-principles study of electronic and structural properties of CuO. *Phys. Rev. B* **84**, 115108 (2011).
65. Mostofi, A. A. et al. wannier90: A tool for obtaining maximally-localised Wannier functions. *Comput. Phys. Commun.* **178**, 685 (2008).
66. Wu, Q. S., Zhang, S. N., Song, H.-F., Troyer, M. & Soluyanov, A. A. WannierTools: An open-source software package for novel topological materials. *Comput. Phys. Commun.* **224**, 405 (2018).

Author contributions

Y.W. and X.Z. contributed equally to this work. L.C. proposed and conceived this project. Y.W. and H.L. contributed to the experiment. X.Z., J.S., L.Y., J.Z., and F.M. performed the theoretical calculations. Y.W., L.C., K.W., X.Z., J.S., P.C., Y.Z., and B.F. analyzed and discussed the data. Y.W., X.Z, L.C., B.F., and J.S. wrote the manuscript with the input and comments from all co-authors.

Competing interests

The authors declare no competing interests.

Additional information

Supplementary information The online version contains supplementary material available at https://doi.org/10.1038/s41467-024-55372-x.

Correspondence and requests for materials should be addressed to Baojie Feng, Jiatao Sun or Lan Chen.

Peer review information *Nature Communications* thanks the anonymous reviewer(s) for their contribution to the peer review of this work. A peer review file is available.

Reprints and permissions information is available at http://www.nature.com/reprints

Publisher's note Springer Nature remains neutral with regard to jurisdictional claims in published maps and institutional affiliations.